Journal of Physics: Conference Series

PAPER • OPEN ACCESS

Effects of ambient turbulence on the near wake of a wind turbine

To cite this article: Yusik Kim *et al* 2016 *J. Phys.: Conf. Ser.* **753** 032047

Effects of ambient turbulence on the near wake of a wind turbine

Yusik Kim, Eva Jost, Galih Bangga, Pascal Weihing, Thorsten Lutz
Institute of Aerodynamics and Gas Dynamics (IAG), University of Stuttgart,
Pfaffenwaldring 21 Stuttgart 70569, Germany

E-mail: `kim@iag.uni-stuttgart.de`

Abstract. Developments of the near wake behind the Avatar research turbine (radius of 102.88 m) in ambient turbulence are investigated using high fidelity numerical simulations. A moderate level of background turbulence with a wide range of scales, which has not been considered in the previous studies is applied. With ambient turbulence, a significant impact on the near wake development is observed. The mean velocity profile becomes Gaussian after 450 m distance downstream, which is a demarcation between the near and the far wake. From the spectral analysis of the wake, clear peaks in the spectra are observed at the blade passing frequency, but the distributions of the peak extend into a wide range of frequency domain. Such aspects provide useful information in classifying periodic and stochastic fluctuations, and their contributions to the momentum mixing in the wake.

1. Introduction

Wind turbines take the kinetic energy from the wind, and thus the velocity reduces and turbulence increases in the wake behind the turbines. Such deviations recover to the freestream state in a certain distance downstream. Understanding how the wake evolves is a challenging task because it depends on many factors such as the tip-speed-ratio, scale and magnitude of ambient turbulence. Recently, Sørensen et al. [1] suggested an analytical formulation to estimate a near wake distance (defined as a distance from the turbine to the location at which the velocity deficit profile becomes Gaussian) based on their numerical simulations. From wind tunnel measurements, Lignarolo et al. [2] reported that mutual inductance and its breakdown are responsible for the turbulence mixing rate in the wake. Mutual inductance is an interaction of a helical tip vortex pair, also known as leapfrogging instability, which facilitates a transition to turbulence. Felli et al. [3] reported that it is a main instability of the propeller wake. These studies provided a practical tool and insightful understanding on the evolution of the wind turbine wake. However they either applied a point source of disturbances near the tip [1, 4], or a low level of ambient turbulence [2], which are not common for the wind turbine operating condition in practice. Therefore, the main objectives of the study are twofold: the first is to quantify the near wake distance with ambient turbulence which contains a wide range of scales; the second is to characterize the mutual inductance and its breakdown in a moderate level of turbulence. To achieve the objectives, three stepwise numerical simulations were designed: the first is to quantify upstream turbulence (Sec. 3.1); the second is to identify resolution dependence of tip vortex dynamics with laminar inflow (Sec. 3.2); the last is to combine these two cases to investigate effect ambient turbulence on the near wake development (Sec. 3.3). The structure

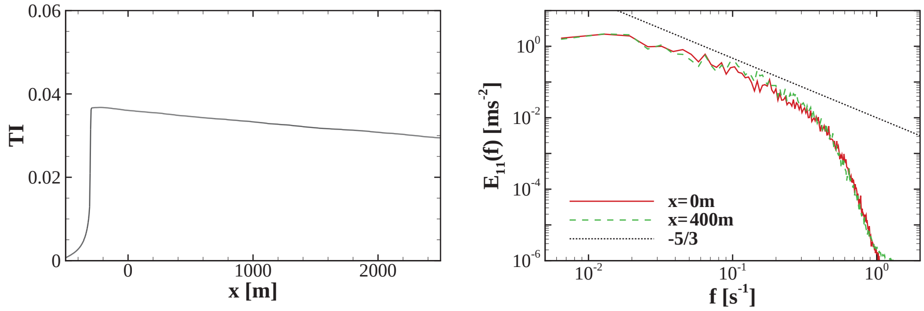

Figure 1. Turbulence intensity TI (left), and 1-D energy spectra for the streamwise velocity fluctuations E_{11} at $x = 0, 400$ m without a turbine (right).

of the paper is composed with the description of numerical set-up and input parameters in Sec. 2; results and discussions on the three cases in Sec. 3; and conclusion in Sec. 4.

2. Methodology

The block structured compressible solver FLOWer [5] with relevant extensions [6] at the Institute of Aerodynamics and Gas Dynamics (IAG), University of Stuttgart was used. For a wind turbine model, the AVATAR research turbine was adopted, which was designed within the AVATAR project [7] for up-scaling wind turbines towards 10-20 MW. The radius of the turbine was $R = 102.88$ m, and the blade was comprised with six DU-airfoils. The radial variations of thickness, chord and twist angle were optimized to have a large power production and a low induction, while the bending momentum maintains the same [8]. In the current study, a pure rotor, i.e., three blades without a nacelle and tower, was considered. The raw data for turbine geometry are openly accessible [7].

Block structured meshes were separately generated for the blade and background, and they were combined without sacrificing the quality of the meshes by using the Chimera overlapping grid technique [9]. The mesh convergence tests were performed separately: for the blade mesh, a C-type mesh around the blade was adopted with $[280 \times 128 \times 192]$ cells in the chord, wall-normal and spanwise directions [10, 11]; for ambient turbulence, a uniform mesh was applied with 4 m resolution at which background turbulence needs to be resolved [12]. Kim et al. 2016 [12] reported that the resolution needs to meet the condition of $L/\Delta x \geq 20$ to capture characteristic behaviours of homogeneous isotropic turbulence (HIT), i.e. decay rate of turbulence kinetic energy, inertial subrange etc, where L is the turbulence length scale and Δx is the cell size. As $L = 89.53$ m in the current study, 4 m resolution satisfies the condition. When flow is bounded by the ground, a wall distance is the dominant length scale while a turbulence length scale is the only relevant length scale in HIT, i.e. current study. This may be the reason that many studies in the atmospheric science adopted even coarser resolutions than the current one. A local refinement near the turbine was applied for a transition from blade to the background meshes.

The operating conditions were set as freestream velocity $U_\infty = 10.5$ ms^{-1}, rotation speed was 9.02 r.p.m. resulting in the tip-speed-ratio $\lambda = 9.26$, and input turbulence intensity $TI_0 = 0.05$. The pitch angle was set to zero and no wind shear was considered, i.e. uniform mean inflow velocity. A uniform velocity and constant pressure were set at the inlet and outlet boundaries respectively. A second order dual time stepping method was adopted for the time discretization. A five-stage Runge-Kutta scheme was used for every inner-iteration, and 45 inner-iterations were applied at each time step. The time step applied for all calculations was set for the azimuthal variation of the blade to be $2°$ per time step, namely $\Delta t = 2°$. As a turbulence model, $k-\omega$ based IDDES model [13] was applied, and no transition model was considered, i.e. fully turbulent.

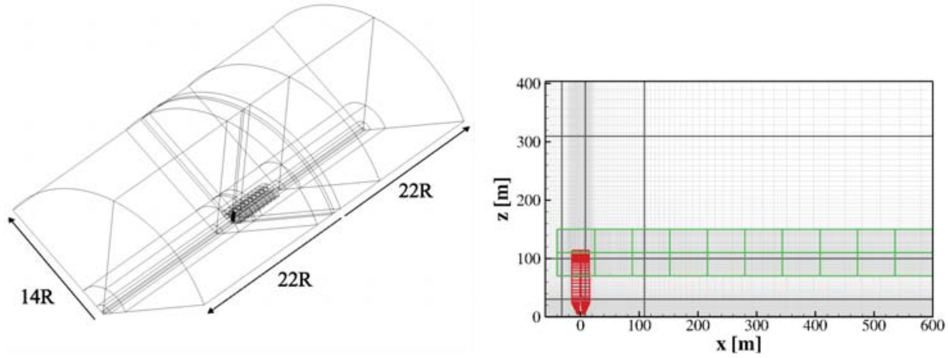

Figure 2. The size of domain (left), and local refinement region near the tip vortex region (right) for the one-third model. The region highlighted with green colour is the tip-vortex refinement region.

3. Results and discussion

3.1. Quantification of upstream turbulence

To generate turbulence inflow, the Mann model [14] was provided by the DTU WIND. The set of input parameters was defined for $TI_0 = 0.05$, and they were (L [m], Γ [-], $\alpha\epsilon^{2/3}$ [$\mathrm{m^4 s^{-2}}$]) $=$ $(89.53, 0.0, 0.20)$ respectively. The size and the number of grid points of the Mann turbulence box were $[2048 \times 2048 \times 2048]$ $\mathrm{m^3}$ and $[512 \times 512 \times 512]$ respectively.

To quantify background turbulence, an empty box without the turbine was simulated. The computational domain size was set to $[3308 \times 2000 \times 2000]$ $\mathrm{m^3}$ in the streamwise (x) and two crossflow (y, z) directions. The inlet boundary was located at $x = -544$ m, and the generated turbulence was imposed at $x = -300$ m using momentum source term [15, 16]. The imposed isotropic turbulence decays naturally as it convects to the downstream region due to no shear, and thus effective TI at which the turbine will be located would be smaller than TI_0. To quantify effective TI in the downstream region, the resolved TI is shown in Fig. 1 (left). At the the turbulence plane $x = -300$ m, TI increases rapidly across this point. As the x increases, TI decays, and the effective TI at the turbine location $x = 0$ m is $TI = 0.036$.

Spectral analysis for background turbulence is also of interest. The energy spectrum E_{ij} is defined as,

$$\begin{aligned} C_{ij}(s) &= \frac{1}{T}\int_0^T u'_i(t)u'_j(t+s)dt, \\ E_{ij}(f) &= \frac{1}{\pi}\int_{-\infty}^{\infty} C_{ij}(s)e^{-ifs}ds, \end{aligned} \tag{1}$$

where s is the temporal separation, C_{ij} is the two-point correlation and $i, j = 1, 2, 3$. Normally, C_{ij} and E_{ij} are defined in space, i.e. $C_{ij}(r)$ and $E_{ij}(\kappa)$. For statistically homogeneous turbulence, they can be approximated in time as in Eq. (1) by the Taylor's hypothesis. The energy spectra calculated using the streamwise velocity fluctuations $E_{11}(f)$ are shown in Fig. 1 (right). In the current study, imposed turbulence does not present unphysical peaks in the spectra, and the $-5/3$ slope of the inertial sub-range is captured for nearly an order of magnitude in frequency range, i.e. $0.04 < f < 0.4\,\mathrm{s^{-1}}$. The current method to present background turbulence is therefore suitable in this study because TI changes mildly along the x direction, and a relatively wide range of scales are resolved.

3.2. Effect of resolutions on tip-vortex dynamics

As mentioned, helical tip-vortices and their interactions in the wake are important mechanisms for the near wake development. This section is to find resolution which presents a converged solution for the tip-vortex dynamics i.e. vortex merging is not induced by the resolution effect. For this, three mesh resolutions (2, 1 and 0.5 m) near the tip region were tested, see Fig. 2 (right). A laminar inflow was applied to exclude the impact of background turbulence, and a one-third model was adopted to save computational cost see, Fig. 2 (left). The resolution for the background mesh increased with the resolution for the tip vortex mesh in order to have smooth transition between these two meshes. The finest background mesh consisted of $[380 \times 192 \times 160]$ cells in the streamwise, radial and circumferential directions. As only a one-third model was simulated, the periodic boundary condition was adopted in the radial direction.

The integrated force distributions along the blade are shown in Fig. 3. It appears that these radial distributions are not sensitive to the resolutions in the tip region. This implies that the circulations generated near the tip are almost the same for three resolutions, and so are the initial conditions for helical tip vortices in the wake. It is noted that the blade mesh maintained the same. The z component of vorticity contours are presented in Fig. 4. With 2 m resolution, tip-vortices are not clearly presented and the radius of the vortices is too large for it to be individually captured. As resolution increases, the radius of each vortex decreases and its shape becomes circle.

To quantify the tip-vortex characteristics, several important properties are calculated, see Fig. 5. A similar analysis was reported from our group for the MEXICO rotor [17]. Though substantial difference in qualitative contour in Fig. 4, the loci of the peak vorticity value for all three resolutions are very similar each other, see Fig. 5 (top-left). Note that tip-vortices for $x > 180$ m are difficult to identify with 2 m resolution from the contour. In Fig. 5 (top-right), circulations Γ_c on each tip-vortices were calculated by integrating z component vorticity, $\Gamma_c = \int\int_A \omega_z dA$. The integrated surface was determined as $\int\int_A dA = \pi b^2/2$, where b was the distance of neighbouring vortices. Γ_c at the first vortex for all three cases are close each other, and this is consistent with Fig. 3. From the second vortex, Γ_c with 2 m resolution tends to be under-predicted about 10% compared with those with 1 and 0.5 m resolutions.

The peak values for each tip-vortex ω_p are also shown in Fig. 5 (bottom-left). Unlike the loci of tip-vortices, there is no indication for ω_p to be converged as the resolution increases. However, our interest is whether the tip-vortex dynamics, e.g. tip-vortex interaction and its breakdown, is captured independently to the resolution. To assess this, studies on two co-rotating vortices were reviewed because each of neighbouring two-vortices within the system of helical tip-vortices resembles the former. Brandt and Nomura [18] reported that two co-rotating vortices remain

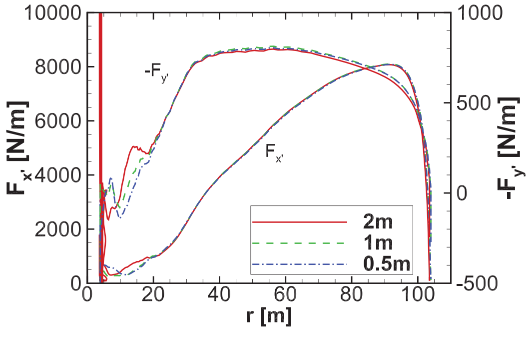

Figure 3. Radial distributions for disc-normal ($F_{x'}$) and azimuthal ($F_{y'}$) forces from the one-third model.

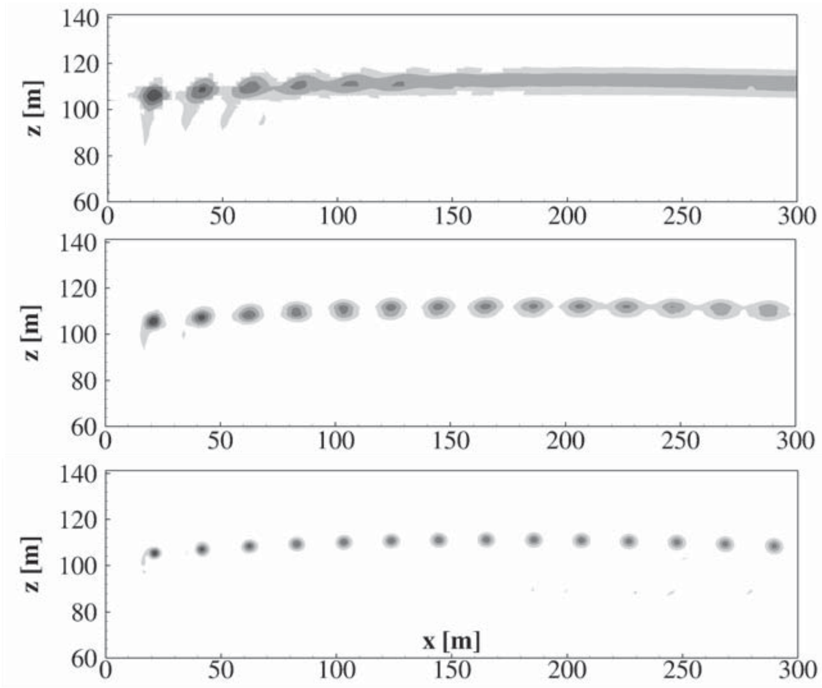

Figure 4. Tip vorticity contour normalised by the maximum peak vorticity. Three levels of resolutions are applied: 2 (top), 1 (middle) and 0.5 (bottom) m. Five colour levels are used between the peak and 10% of the peak vorticity values.

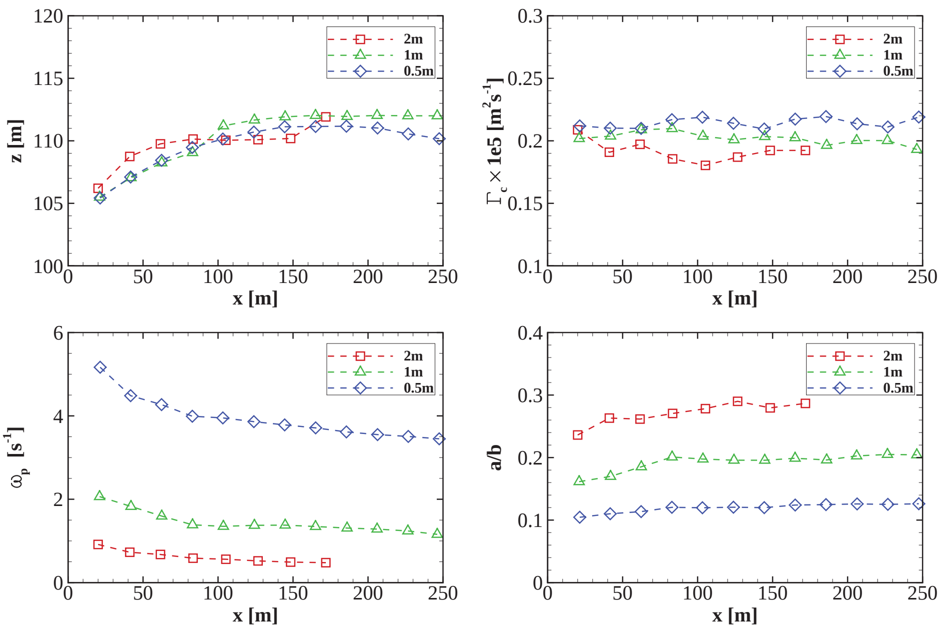

Figure 5. Loci of tip vortices (top-left), circulation Γ_c (top-right), peak vorticities ω_p (bottom-left) and vortex radius to distance ratios a/b (bottom-right).

separated for $a/b < 0.235$, where $a = (\Gamma_c/(\pi\omega_p))^{1/2}$ is the vortex core radius. Therefore, it would be interesting to calculate a/b for the current case to investigate the effect of resolution on the tip-vortex dynamics in the near wake. The calculated aspect ratio a/b is shown in Fig. 5 (bottom-right). Only cases with 1, 0.5 m resolution present $a/b < 0.235$, and a/b increases as resolution decreases. To conclude, 1 m resolution of the wake mesh would be sufficient to achieve the mesh independent solution in terms of the tip-vortex dynamics with the laminar inflow.

3.3. Full rotor simulation with ambient turbulence

Based on resolution tests in Sec. 3.2, a full wind turbine with ambient turbulence was simulated. The domain size was set to $[2000 \times 2000 \times 2000]$ m^3 and the turbulence plane was located at $x = -300$ m. The rotating axis was aligned with the x axis and located at the origin, which was at a distance of 1000 m from the inlet boundary. A local refinement mesh was applied between background and wake meshes, see Fig. 6. 1 m resolution was extended upto $x = 600$ m resulting the total number of cells were 119×10^6.

Fig. 7 (top) shows an instantaneous vorticity contour in the wake region. Structure of tip-vortices near the turbine are significantly different those with from the laminar inflow in Fig. 4 (middle). Tip vortex starts to interact (mutual inductance), with their neighbouring vortices at $x \approx 100$ m, and the organised structure is destroyed after $x = 200$ m. Large eddies in ambient turbulence are also visible around the wake. The iso-surface of λ_2 is shown in Fig. 7 (bottom). Tip and hub vortices are clearly shown near the turbine, and they breakdown to rich and complicated structures soon after the organised motions are disturbed by external turbulence.

The mean velocity, streamwise variance and shear stress profiles at several downstream locations are shown in Fig. 8. Sharp gradients near the tip are observed in U/U_∞ at $x = 50$ m, and the profiles become nearly Gaussian after $x = 450$ m. Thus near wake distance for the current case is approximately 450 m based on [1]. For $u'u'/U_\infty^2$ and $u'w'/U_\infty^2$ profiles, strong peaks are observed near the tip region. These peaks propagate toward in- and outward directions as x increases, and they start to merge each other for $x \geq 450$ m. The profiles shown in the figure are unconditionally averaged, and thus $u'u'/U_\infty^2$ and $u'w'/U_\infty^2$ are contributed by both periodic motion for the blade passage and stochastic fluctuations for turbulence. As only the stochastic part of $u'w'/U_\infty^2$ enhances the momentum mixing in the wake [2], it is important to

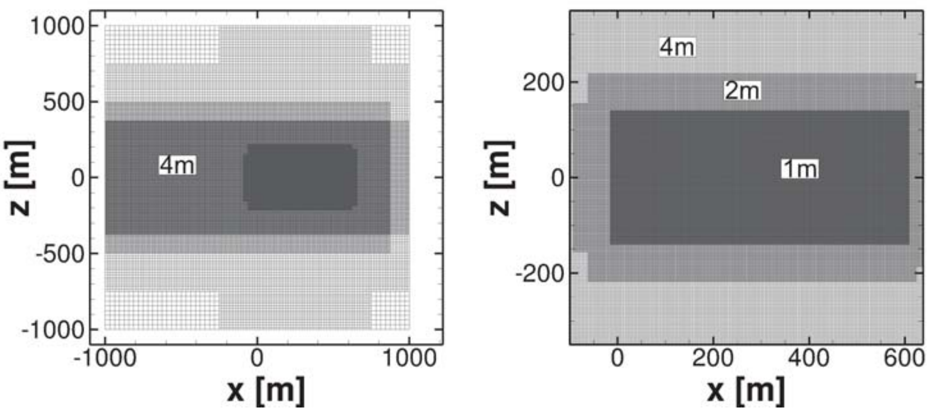

Figure 6. Mesh topology for the full model: overall view (left) and local refinement near the turbine (right). Turbine mesh is not included for clarity.

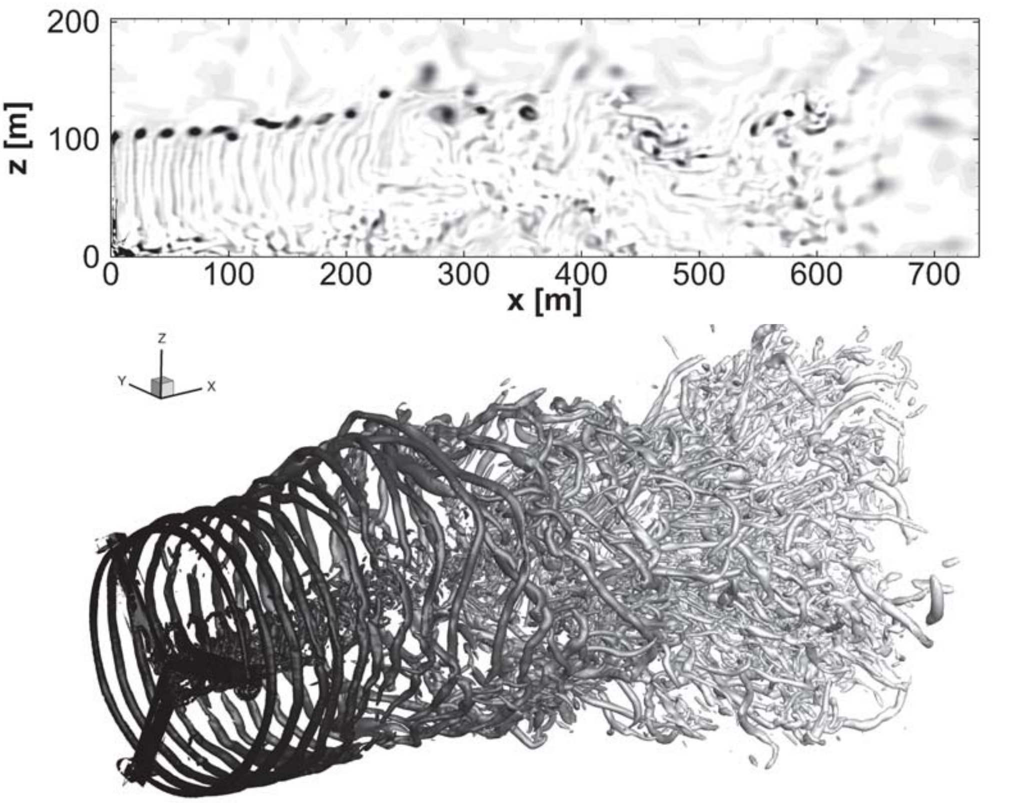

Figure 7. y component of vorticity contour using 21 levels are used for $\omega_z = 0.01 - 1$ [s^{-1}] (top) and iso-surface of λ_2 criteria with colour changing bright as x increases (bottom).

classify contributions from the periodic and stochastic motions to $u'w'/U_\infty^2$. To analyse these two contributions, the shear stress spectra $E_{13}(f)$ are calculated using Eq. (1). The weighted spectra $fE_{13}(f)$ at different radial and downstream positions are shown in Fig. 9. The maximum sampling frequency is $f_{\max} = 1/(2\Delta t_s) = 6.77$ s^{-1}. The total sampling time is $T_s = 106$ s, and the convective distance by the freestream velocity U_∞ during T_s is 1110 m, which sufficiently covers the region of $0 \leq x \leq 600$ m.

Close to the turbine ($x = 50$ m), clear peaks are identified at f_1 and f_2 where f_n are the harmonics of the blade passing frequency, see Fig. 9 for definition. For $x \geq 150$ m, the peaks are rapidly dissipated, and no clear peak is observed even at f_1. As x increases, a wider range of $-3/2$ slope which corresponds to the inertial sub-range, is captured and it is $0.03 < f < 0.4$ s^{-1} at $x = 450$ m. In regard to the classification of periodic and stochastic fluctuations, three important aspects are drawn: a) multiple harmonics are observed. Thus considering only the first harmonic would not be sufficient for the classification; b) the peak frequencies are identical with the harmonic frequencies. Thus filtering frequencies for the classification can be specified without knowing the solution; c) the peaks are distributed in a relatively wide frequency range. The tail for the first peak reaches the other side of the tail for the second peak, see Fig. 9, $x = 50$ m. Thus filtering the signal only at distinctive frequencies would not differentiate the periodic and stochastic motions. The last aspect has not been reported in the previous studies, which is important in the classification.

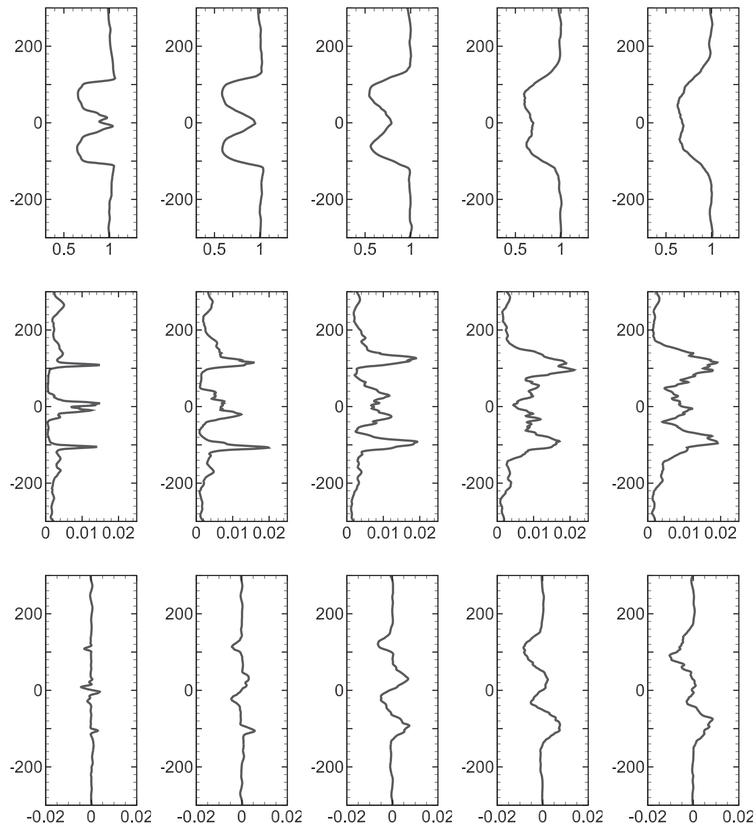

Figure 8. Unconditionally averaged wake profiles at different downstream locations at $x = 50, 150, 300, 450, 600$ m from left to right: Mean velocity U/U_∞ (top), streamwise variance $u'u'/U_\infty^2$ (middle), Reynolds shear stress $u'w'/U_\infty^2$ (bottom). y axis is the z-direction in [m].

4. Conclusion

The AVATAR reference turbine is simulated with a moderate level of ambient turbulence ($TI = 0.036$). To quantify upstream turbulence and a resolution requirement in the tip region, a case for an empty box, and a one-third model with the laminar inflow are set separately. The empty box case shows that ambient turbulence contains a wide range of scales, and the one-third model case suggests 1 m resolution to capture the tip vortex dynamics in the wake.

A full turbine simulation with the turbulent inflow is performed. The mean velocity profiles in the wake present a nearly Gaussian distribution after $x = 450$ m, which indicates the near wake distance [1]. The shear stress spectra $E_{13}(f)$ are calculated to identify characteristics of periodic and stochastic motions, because they are important for the momentum mixing. The analysis shows that the peak frequencies are identical with the harmonics of the blade passing frequency. Also peaks are distributed in relatively wide frequency range which makes filtering out the periodic motions difficult with using a few distinctive modes. Further classification between the periodic and stochastic motions based on calculated $E_{13}(f)$ is planned for the future work including additional cases with higher levels of ambient turbulence .

Acknowledgments

This project has partially received funding from the European Union's Seventh Programme for research, technological development and demonstration under grant agreement No FP7-

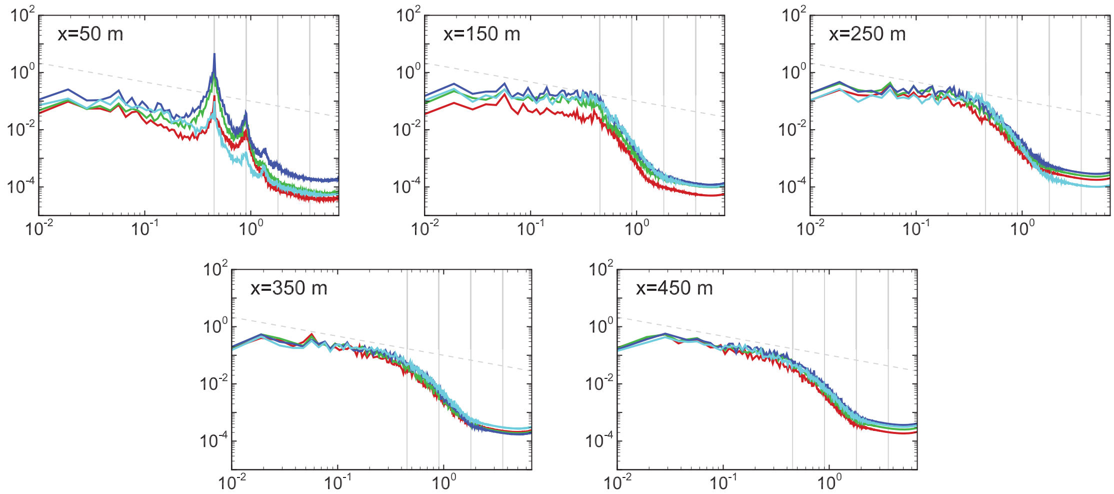

Figure 9. Weighted spectra of shear stress $fE_{13}(f)$ [m^{2}s^{-2}] over frequency f [s^{-1}] at different downstream locations: $x = 50, 150, 250, 350, 450$ m. Different colours represents different radial distance from the hub: $z = 90$ (red), 100 (green), 110 (blue) and 120 (cyan) m. Grey vertical-lines are harmonics of the blade passing frequency $f_n = n3/T$ where T is the period of one revolution and $n = 1, 2, 3, 4$. Grey dashed-line is $-2/3$ slope.

ENERGY-2013-1/no. 608396.

References

[1] Sørensen JN, Mikkelsen RF, Henningson DS, Ivanell S, Sarmast S and Andersen SJ 2015 *Phil. Trans. Royal Soc. London A: Math. Phys. Eng. Sci.* **373**
[2] Lignarolo LEM, Ragni D, Scarano F, Simão Ferreira CJ and van Bussel GJW 2015 *J. Fluid Mech.* **781** 467–493 ISSN 1469-7645
[3] Felli M, Camussi R and di Felice F 2011 *J. Fluid Mech.* **682** 5–53
[4] Ivanell S, Mikkelsen R, Sørensen JN Henningson D 2010 *Wind Energy* **13** 705–715
[5] Kroll N, Rossow CC, Schwamborn D, Becker K, Heller G 2002 *ICAS 2002 Congress*
[6] Schulz C, Fischer A, Weihing P, Lutz T and Krämer E 2015 *High Perform. Compt. Sci. Eng. 15, Springer*
[7] AVATAR 2013 (accessed 24 Feb 2016) URL `http://www.eera-avatar.eu/home/`
[8] Sieros G et al 2015 AVATAR deliverable D1.2 - Reference blade design
[9] Chesshire G and Henshaw WD 1990 *J. Comput. Phys.* **90**
[10] Bangga GSTA, Lutz Th and Krämer E 2015 *EAWE PhD Sminar*
[11] Sørensen NN et al 2014 AVATAR deliverable D2.3 - Power curve predictions
[12] Kim Y, Weihing P, Schulz C and Lutz Th 2016 *J. Wind Eng. Ind. Aerodyn.* **156** 41–49
[13] Shur ML, Spalart PR, Strelets MK and Travin AK 2008 *Int. J. Heat Fluid Flow* **29** 1638–1649
[14] Mann J 1994 *J. Fluid Mech.* **273** 141–168
[15] Troldborg N, Sørensen JN, Mikkelsen R and Sørensen NN 2014 *Wind Energ.* **17** 657–669
[16] Schulz C, Hofsäß M, Anger J, Rautenberg A, Lutz Th, Cheng PW and Bange J 2016a *TORQUE 2016*
[17] Schulz C, Meister K, Lutz T and Krämer E 2016b *New Results in Numerical and Experimental Fluid Mechanics X* (Springer) pp 871–882
[18] Brandt LK and Nomura KK 2007 *J. Fluid Mech.* **592** 413–446